Corrosion mechanisms of Al2O3-SiC-C refractory castables by iron and slag based on post-mortem analysis of industrial samples

Sina Darban, Laurent Cassayre, Simon Chiartano, Laurie Lacarrière, Martin Cyr, Cédric Patapy, Pascal Prigent

Open Ceramics 16 (2023) 100453

Contents lists available at ScienceDirect

Open Ceramics

journal homepage: www.sciencedirect.com/journal/open-ceramics

Corrosion mechanisms of Al_2O_3-SiC-C refractory castables by iron and slag based on post-mortem analysis of industrial samples

Sina Darban [a,*], Laurent Cassayre [b], Simon Chiartano [c], Laurie Lacarrière [a], Martin Cyr [a], Cédric Patapy [a], Pascal Prigent [c]

[a] Laboratoire Matériaux et Durabilité des Constructions, INSA/UPS Génie Civil, Université de Toulouse, CEDEX 04, 31077, Toulouse, France
[b] Laboratoire de Génie Chimique, Université de Toulouse, CNRS, INP, UPS, 31077, Toulouse, France
[c] TRB, 69150, Decines Charpieu, France

ARTICLE INFO

Handling Editor: Dr P Colombo

Keywords:
Al_2O_3-SiC-C castables
Post-mortem
Corrosion
Microstructure
Thermodynamics

ABSTRACT

The Al_2O_3-SiC-C or ASC castables are used in the main runners of blast furnaces. Most of the papers published to date focus on laboratory corrosion tests because access to the post-mortem samples of ASC castables is difficult. However, investigation of post-mortem samples is crucial in reducing the wear of ASC castables. The main runner is divided into the turbulence, middle, and non-turbulence zones. The microstructures of post-mortem samples located in working linings of different zones were investigated by SEM/EDS technique. The thermodynamic simulations were carried out in different systems, such as slag/refractory and iron/refractory, using the FactSage software. The SEM/EDS results showed the formation of phases with low melting points, such as gehlenite and anorthite, together with spinel solid solutions in the matrix and calcium dialuminate near the alumina aggregates. The thermodynamic simulations showed that slag and iron tend to react with alumina and silicon carbide, respectively.

1. Introduction

Al_2O_3-SiC-C or ASC refractories are used in the runners of blast furnaces because of their excellent thermal shock resistance, outstanding corrosion resistance, and intrinsic properties, such as high chemical and oxidation resistance [1–3]. Alumina is a primary aggregate in ASC castables because of its excellent hardness, high corrosion resistance, and chemical stability [4,5]. Silicon carbide (SiC) is one of the main additives in ASC castables due to its high resistance to thermal shock and corrosion [5,6]. The SiC can be formed in situ or added directly to the composition of the ASC castables [6,7]. Carbon is implemented for its non-wettability with the slag in the ASC castables matrix [7,8]. Carbon could react with Al or Si additives and create ceramic phases like SiC, Al_4C_3, SiC, Al_4O_4C, and Al_4SiC_4, improving the mechanical properties of ASC castables [6].

Some studies have contributed insight into the effect of each component of ASC castables and helped to improve their corrosion resistance [3,9–13]. Sarpoolaky et al. [14] studied the effect of different alumina aggregates (WFA,[1] TA,[2] BFA[3]) on the corrosion resistance of low cement castables (LCC[4])and showed that titanates in the BFA grain formed new phases and densified the castable. As a result, the level of infiltration of slag was less than for WFA and TA. On the other hand, an outstanding level of liquid phase from BFA dissolved in the slag and intensified the corrosive wear of BFA aggregates. Fan et al. [15] showed that the morphology of the SiC affected the mechanical properties of ASC refractories. The strength of ASC refractories was associated with the morphology of SiC in the matrix. Elongated SiC whiskers were more advantageous for high-temperature mechanical properties of refractories than SiC particles with spherical shapes. In another study, Chen et al. [16] investigated the effect of the microstructure of in-situ SiC whiskers on the mechanical properties of alumina-carbon-based refractories. Their results showed that the formation of SiC whiskers enhanced the mechanical properties of alumina-carbon refractories.

Other studies have been dedicated to investigating the corrosion

* Corresponding author.
E-mail address: darban@insa-toulouse.fr (S. Darban).

[1] White fused alumina.
[2] Tabular alumina.
[3] Brown fused alumina.
[4] Low carbon containing castables.

https://doi.org/10.1016/j.oceram.2023.100453
Received 14 July 2023; Received in revised form 31 August 2023; Accepted 31 August 2023
Available online 4 September 2023

mechanism of ASC castables in laboratory conditions. Zou et al. [7] studied the corrosion behaviour of Al_2O_3-SiC-SiO_2-C (ASSC) materials based on laboratory corrosion tests under an inert atmosphere (Ar). According to their results, CaO and MgO from slag reacted with mullite and produced new phases such as gehlenite ($Ca_2Al_2SiO_7$) and akermanite ($Ca_2MgSi_2O_7$). These low melting point phases increased the speed of infiltration of slag. Therefore, the corrosion resistance of ASC castables decreased.

In another laboratory study, Wang et al. [6] studied the corrosion resistance of ASC castables with different coal tar pitch (CP) contents in a reductive atmosphere (RA), a weak reductive atmosphere (WRA), and an oxidizing atmosphere (OA). According to their results, the pore size and the apparent porosity of the ASC samples were higher in the WRA than in OA and RA. The penetration of slag in OA and RA was around 4 mm, but in the WRA, the penetration of slag was the highest (7 mm). In the OA, the oxidation of SiC generated SiO_2, which dissolved into the slag and increased its viscosity. The oxidation of SiC formed amorphous SiO_2, and the resulting SiO_2 reacted with Al_2O_3 to form mullite. Hence, the formation of low melting point phases and mullite on the surface of ASC samples raised a dense structure and limited the oxidation of SiC.

In contrast, in the WRA, the SiO_2 that formed provided channels for the slag to penetrate the matrix of ASC castables. Wang et al. found that, in WRA, only a limited amount of SiO_2 dissolved into the slag and did not affect its viscosity. Their SEM results showed the spinel grains within the slag zone and a limited amount of calcium hexaluminate (CA_6) in a continuous layer on the surface of corundum aggregates. Nevertheless, there has been no thermodynamic study on the mechanisms of their explanations that could give results comparable to the experimental findings from the laboratory corrosion tests.

A thermodynamic approach may assist the understanding of the chemical reactions between slag and ASC castables. For instance, the ternary phase diagram of Al_2O_3-CaO-SiO_2 shown in Fig. 1 provides a general overview of the possible phase formation when slag (predominantly composed of CaO and SiO_2) reacts with alumina, which is one of the main components of the refractory. Here, the slag composition (red dot in Fig. 1) is in the gehlenite region of the ternary phase diagram, with a melting point of about 1400 °C. As represented by the green arrow, the mixing of slag with Al_2O_3 changes the melting point of the slag and eventually the nature of the main solid phase after cooling, with the possible sequential formation of cementitious calcium aluminate, e.g., calcium monoaluminate ($CaAl_2O_4$), calcium dialuminate ($CaAl_4O_7$), and calcium hexaluminate ($CaAl_{12}O_{19}$). Although the use of such a diagram can provide qualitative information, computational tools based on the prediction of chemical equilibria through Gibbs energy minimization allow a much more quantitative approach to be used, with the possibility of taking the complexity of the industrial chemical systems, composed of many chemical elements, into account.

Furthermore, it is informative to perform corrosion tests in laboratory conditions to understand the corrosion mechanisms of ASC castables. However, the conditions of the laboratory tests (atmosphere, temperature, heating rate) can be far from industrial conditions. Therefore, investigating the post-mortem samples exposed to real industrial conditions could be interesting to understand the fundamental needs for improving the next generation of refractory materials. In this study, the post-mortem samples of Al_2O_3-SiC-C (ASC) castables used in the blast furnace's main runner are investigated. The post-mortem study on the ASC castables located in the various zones of the main runner can reveal determining events of their lifetime. Comparing the post-mortem samples of ASC castables located in the working linings of the runner could give important information regarding their chemical and mechanical degradations.

This research focuses on the corrosion mechanism of ASC castables by implementing post-mortem analysis and thermodynamic computations. First, the microstructure of the post-mortem samples of ASC castables from different (turbulence, middle, non-turbulence) zones of the main runner was investigated by SEM/EDS. Next, thermodynamic simulations were performed with the FactSage commercial software. Based on the principle of the main runner of the blast furnace, the

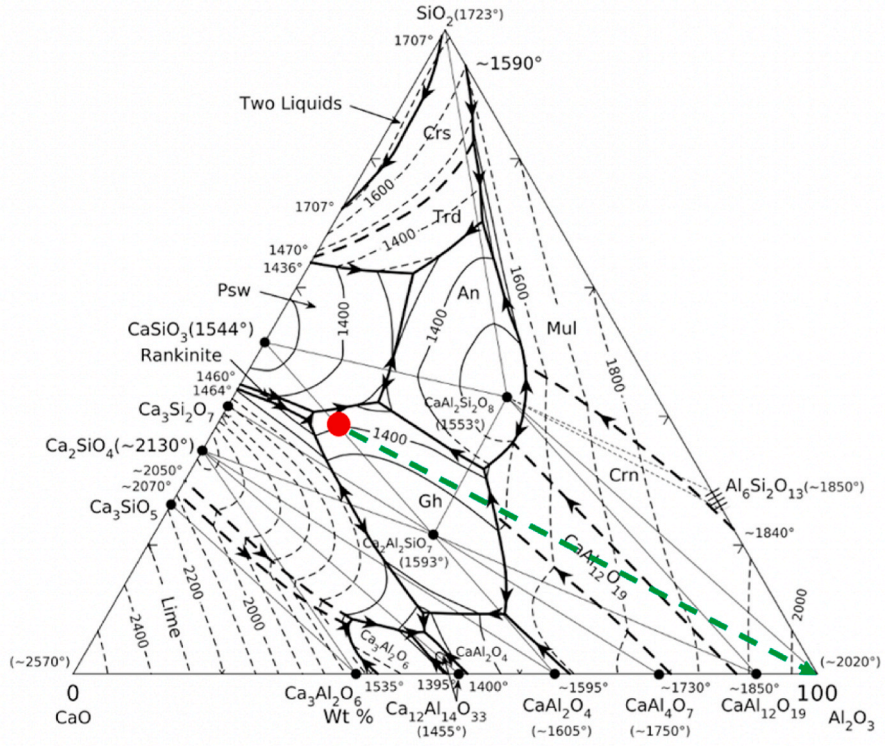

Fig. 1. Ternary phase diagram of Al_2O_3-CaO-SiO_2 [17]. The red dot is the composition of the blast furnace slag studied, and the green arrow show s the direction of the chemical reaction of slag and alumina. Gh-gehlenite, An-anorthite, Trd-tridymite, Crs-Cristobalite, Mul-mullite, Crn-corundum, PSw- Pseudo Wollastonite. (For interpretation of the references to colour in this figure legend, the reader is referred to the Web version of this article.)

thermodynamic computations investigated phase equilibria with the presence of slag or iron in contact with ASC castables at high temperatures and during the cooling steps.

According to local information, the minimum and maximum temperatures of the runner are 1440 °C and 1580 °C, respectively. However, the (average) working temperature measured for the runner is around 1505 °C. Fig. 2 shows a schematic side view of the main runner of the blast furnace. Liquid slag-iron mixture is introduced through the tap hole in the runner (zone A), and slag and iron are separated at the end of the runner (zone C).

The simulation technique is a powerful tool commonly used to analyse and predict the behaviour of fluids, especially in severe environments such as blast furnace runners, where measurement is difficult. Therefore, a computational fluid dynamics (CFD) multiphasic study was carried out to understand the flow distribution of cast iron and slag when the stream arrives at the main iron runner. The model considered comprised the internal walls of the main iron runner, the cast iron, the slag, and an air layer above. ANSYS Fluent software [22] was used with a k-ω SST law for the turbulence, which is a two-equation eddy-viscosity model combining the Wilcox k-omega and the k-epsilon models. This choice was made by considering a low Reynolds number and the stability regarding convergence [19]. Surface tension was considered between the three phases (air/slag/cast iron) to define the interfaces accurately. Fig. 3 indicates the boundaries of this simulation, i.e., inlet and outlet locations. The inlet mass flows of air, slag, and cast iron: 0 kg/s, 20 kg/s and 60 kg/s, respectively, are shown below.

The CFD simulations mesh comprised 6 million cells for the global geometry and a detail of the turbulence zone with special refinement. A non-structured mesh of hexahedral elements, a classical choice for complex designs, was used in this simulation. Fig. 4 below shows the interface results or, in other words, the surface separating one phase from another. The blue surface is the air/slag interface, and the grey is the slag/cast iron interface.

Fig. 5 focuses on the slag volume fraction. A value of 1 (red) means 100% of slag, and 0 (blue) means air (above) or cast iron (below). Between, the gradient shows a mix of these phases. This result is interesting for understanding the phase distribution along the runner. The turbulence zone seems to be a turbulent area with mixed phases. It takes about half the runner's length to obtain full segregation with slag on the top and cast iron under it.

The velocities of cast iron and slag are presented below in Fig. 6. Again, the first part of the runner seems to be the most animated place. The highest velocity is at the center plane or just after the turbulence of the stream. Walls near the turbulence zone are also subjected to relatively high-speed flow. After the middle of the runner, velocities are low. They accelerate once again in the outlets as the section decreases.

To analyse the flow movement in the turbulence zone, where flow is both rapid and mixed, Fig. 7 shows the velocities along the z-axis and highlights the negative values, which indicate back-flow. The results are a high velocity on the "straight" way in the middle after the impact and a big recycling flow in a circle on the sides. These back-flows are almost symmetrical and come back to the beginning of the runner, where they are re-centered. Arrows highlight the circulation of the mixture in this area.

These calculations enable us to understand how the runner works from a hydromechanical point of view. They show that, from left to right (in Fig. 2), the runner is separated into three main parts: a turbulence zone (A), a middle zone (B), and a non-turbulence zone (C). The most worn part of the runner observed in situ is in the turbulence zone (A) since the corrosive media (slag and iron) drain directly from the taphole into the turbulence zone (A). The level of wear in zone A is a determining factor of the runner's lifetime, due to its maximum efficiency in running the flow of molten slag and metal. The slag and iron separate at the end section of the runner, called the non-turbulence (C) zone. Compared to zone A, there is less dynamic motion of melts in zone C, which is considered to be a non-critical zone in the BF's runner. The calculations also show (Fig. 7) that, in the turbulence zone, slag and iron mix in the section, leading to coupled exposure of the runner walls to both phases.

The previous studies by different researchers were dedicated only to laboratory corrosion tests in different atmospheres and with different formulations of ASC castables. Nevertheless, it is quite important to reproduce the actual industrial conditions and their effect on the corrosion mechanisms of ASC castables, especially when the subject concerns the main runner, which contains different corrosive media (slag and iron) with various properties. In addition, as the CFD simulations have shown in the previous parts, the mechanical conditions on the main runner could be drastically different from the controlled conditions of laboratory tests. As a result, the corrosion mechanisms and their effects on the wear of ASC castables could be far from the laboratory results. In this study, the post-mortem samples of ASC castables were studied in terms of microstructural analysis. The post-mortem samples were received from different locations in the main runner after experiencing real working conditions at the industrial site. Thermodynamic calculations were also implemented as a complementary method for indicating the different roles of iron and slag in the corrosion mechanisms of ASC castables through their lifetime.

2. Materials and methods

2.1. Slag and refractory castable

The slag in this study originated from an industrial installation and was not synthesized in laboratory conditions. Table 1 shows the chemical composition of blast furnace (BF) slag used in this study. The major components are (wt.%) SiO_2 37.2, CaO 34.4, Al_2O_3 14. The minor components are (wt.%) MgO 8.8, K_2O 1, SO_2 0.9, TiO_2 0.7, MnO 0.6, Na_2O 0.6, FeO 0.4. Based on CaO/SiO_2, the percentage of basicity is around 0.92%, indicating that the BF's slag is acidic. According to Ref. [18], the liquidus temperature of the blast furnace slag is around 1455 °C; phases (wt.%) at 1350 °C are 18% liquid and 82% melilite; and at 1400 °C are 25% liquid and 75% melilite.

The mineralogical composition of ASC castables is shown in Table 2.

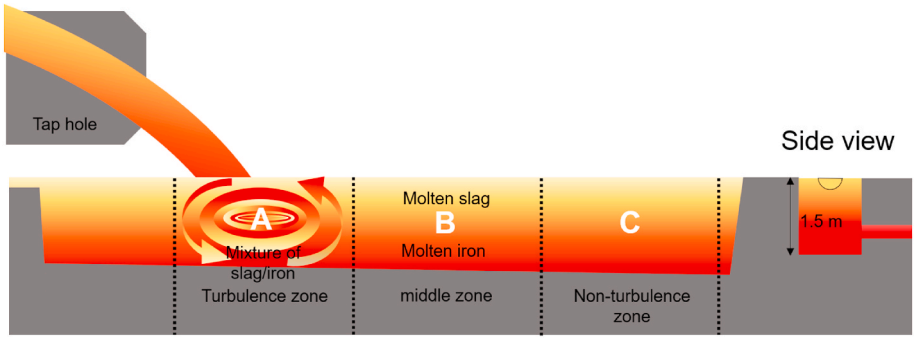

Fig. 2. Schematic view of the main runner of the blast furnace; turbulence zone (A), middle zone (B), and non-turbulence zone (C).

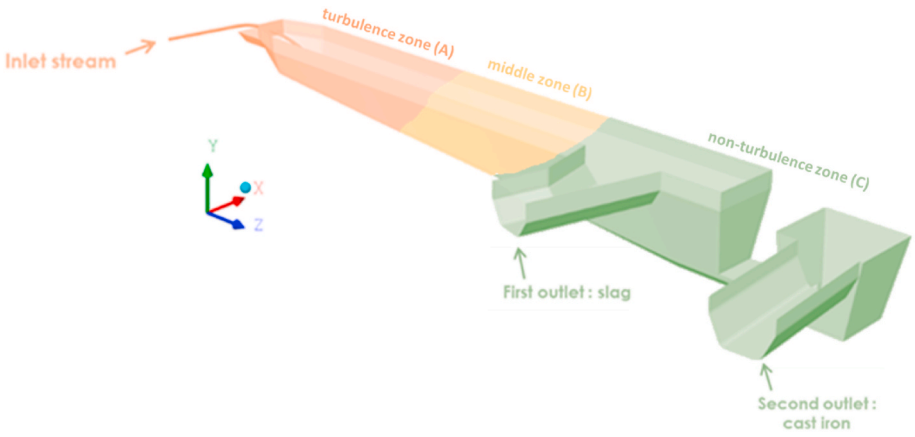

Fig. 3. Main runner of blast furnace CFD simulation boundaries: inlet and outlets.

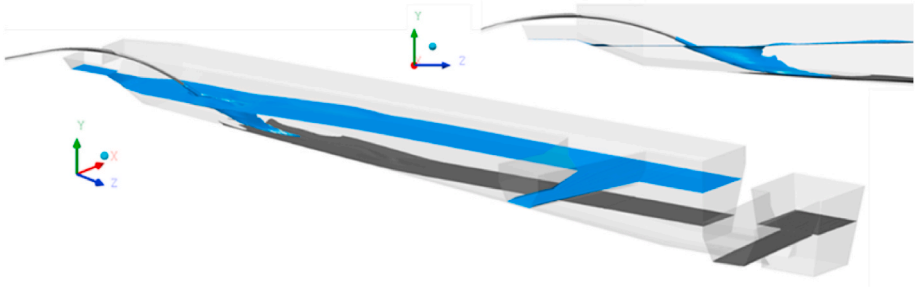

Fig. 4. CFD interfaces results: air/slag (blue) and slag/cast iron (grey). (For interpretation of the references to colour in this figure legend, the reader is referred to the Web version of this article.)

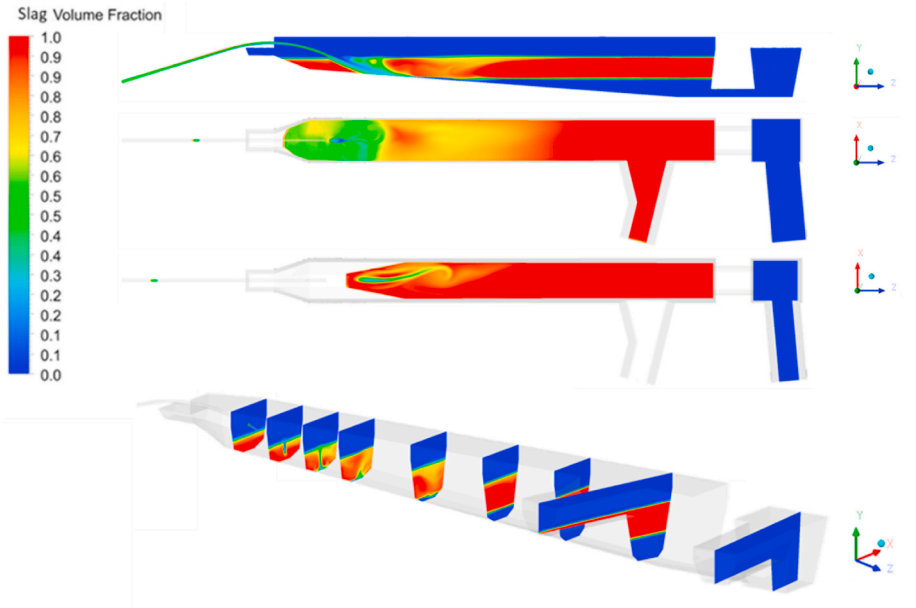

Fig. 5. CFD slag ratio results: the amount of slag in the mixture.

The major components of the castable are (wt.%): 60-65 alumina aggregates (0-1 mm,1-3 mm, 3-5 mm, 5-10 mm), 15-25 silicon carbide (0-200 μm, 0-1 mm), and 8-15 fine alumina (3-6 μm). The minor components are (wt.%): 2-3.5 carbon (carbon black, graphite, pitch), 1-2.5 cement (CAC), 0-2.5 silica fume, 0.5-3 antioxidants (Al, Si, B_4C), and 0.1-0.2 additives for flowability and setting time (citric acid, oxalic acid).

2.2. Selection of the post-mortem bricks of the main runner

The post-mortem Al_2O_3-SiC-C (ASC) castables were received from the industrial partner of this project. Fig. 8 shows schemas of the runner before corrosion (a) and after corrosion (b). Fig. 8(a) shows how slag and iron are divided between the top and bottom of the runner. Thus, the vertical cross-section at the top (zone 1) is air/slag/refractory in the

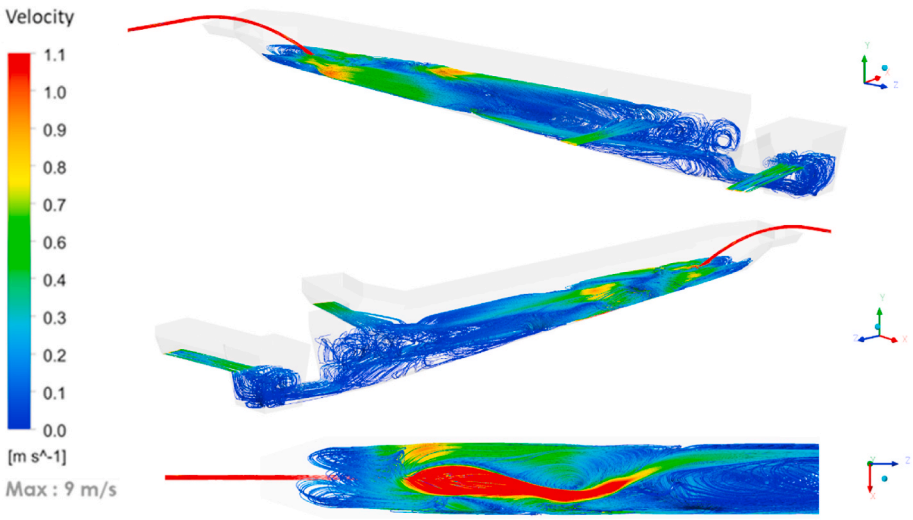

Fig. 6. CFD velocity results: velocity magnitude of the mixture.

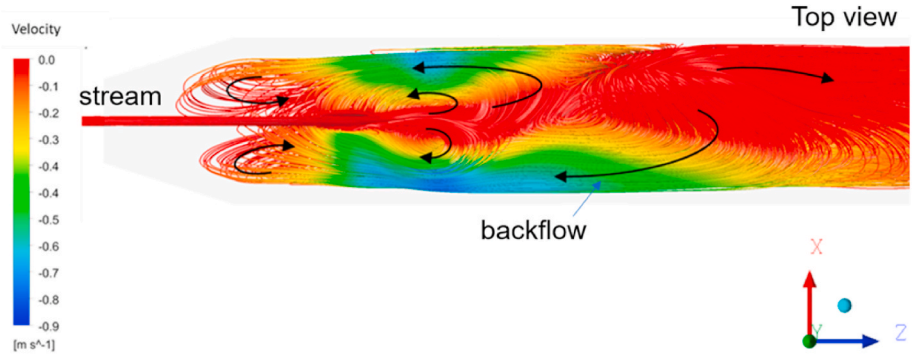

Fig. 7. CFD back-flow results: flow against the tide on the turbulence zone of the blast furnace in the z-direction.

Table 1
Chemical composition of blast furnace slag in wt.%.

SiO_2	CaO	Al_2O_3	MgO	K_2O	SO_2	TiO_2	MnO	Na_2O	FeO	Others	Sum	%B (C/S)
37.2	34.4	14	8.8	1	0.9	0.7	0.6	0.6	0.4	1.4	100	0.92

Table 2
The chemical composition of Al_2O_3-SiC-C (ASC) castables.

Components	wt.%
Brown fused alumina (BFA)	60-65
SiC	15-25
Fine alumina	8-15
Carbon	2-3.5
Cement	1-2.5
Silica fume	0-2.5
Antioxidants	0.5-3
Additives for flowability	0.1-0.2

oxidizing atmosphere. The cross-section (zone 2) at the bottom is slag/iron/refractory with no air, and a reductive (or semi-reductive) atmosphere is present. Fig. 8(b) shows the names given to the (post-mortem) samples (from top to bottom): slag line (sample 1), slag/metal line (sample 2), and metal line (sample 3).

The information regarding the adhesion level of the post-mortem samples is summarized in Table 3. The sample names are based on the zone of the runner and their positions in the linings. Based on macroscopic observation, the most adhered samples which have corrosive agent on their surface are A-2, A-1, B-1, and B-2. Hence, samples A-1, A-2, B-1, and B-2 were investigated from the turbulence zone (A) and middle zone (B) of the main runner. Sample C-1 from the runner's non-turbulence zone (C) was also investigated for comparison. However, macroscopically, the C series sample did not show significant degradation on its surface.

2.3. Preparation of post-mortem samples

A wire saw was used to prevent any damage to the post-mortem bricks during cutting. The post-mortem ASC sample was cut with a length of 25 mm in order to be used for microstructural investigations. Fig. 9 depicts the different sides of the post-mortem brick A-2 as an example for a better understanding of the cutting procedure. Classically, the post-mortem bricks are divided into two sections based on their location during their lifetime: hot face (interacted section) and cold face (non-interacted section). The hot face is where the molten slag (oxides) and iron were in contact with the ASC castables and, as a result, adhered slag and iron are present on the hot face side of the post-mortem bricks. Hence, it could be expected that the most degraded area would be the hot face of the post-mortem ASC bricks.

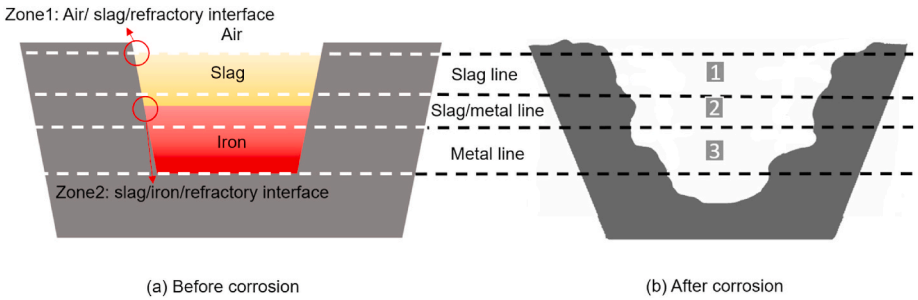

Fig. 8. Schema of the main runner of a blast furnace before (a) and after (b) corrosion. The runner is divided into air/slag/refractory (zone 1) and slag/iron/refractory (zone 2). The post-mortem samples were selected from the slag line (1), slag/metal line (2), and metal line (3).

Table 3
The level of adhesion of post-mortem samples from different zones.

Zone	Sample No.	Lining loc.	Adhesion of corrosive agents
A	1	Slag	++
	2	Slag/iron	+++
	3	Iron	-
B	1	Slag	+
	2	Slag/iron	+
	3	Iron	-
C	1	Slag line	-
	2	Slag/iron	-
	3	Iron	-

Conversely, the cold face is where the brick side was not in contact with any corrosive medium (slag or iron). In general, the cold face is assumed to be the side of the brick facing the safety linings on the back walls of the runner. A thermal gradient could be present in the cold face section, but no chemical degradation was expected to be observed.

As explained above, the cutting procedure was carried out parallel to the thermal gradient and perpendicular to the hot face. Fig. 10 shows post-mortem brick A-2 as an example. The hot face and cold face were located on the lower and upper sides of the brick A-2, respectively. The barrier between adhered slag/iron and the refractory are highlighted all over the sample (line of red dots). In contrast, the border of the cold face on the left side is not distinguishable, and there is no sign of adhered slag/iron. The sample preparation from brick A-2 for SEM/EDS analysis was performed from the interaction zone where the slag and iron were in touch with the ASC refractory, since this zone was the largest (40 cm) degraded part of the post-mortem brick A-2.

The post-mortem samples from zone B (middle of runner) are shown in Fig. 11(a-c). The adhered slag and slag/iron are visible on the surface of samples B-1 and B-2. Nevertheless, there is no visible adhered slag or iron on sample B-3, which was located in the iron line at the bottom of the runner. The same procedure as brick A-2 was repeated for the preparation of samples from post-mortem bricks B-1, B-2, and C-1.

2.4. Thermodynamic simulations with FactSage software

The commercial software FactSage® v8.2 [20] was implemented for the high-temperature thermodynamic calculations. The input chemical compositions of the different parts of the system were as follows.

- The ASC castable composition was (wt.%) Al_2O_3 79.3, SiO_2 2.6, CaO 0.6 and SiC 17.5.
- The blast furnace slag was slightly simplified from the composition provided in Table 1 (wt.%): CaO 35.9, Al_2O_3 14.6, SiO_2 38.7, MgO 9.1, K_2O 1.0, Na_2O 0.6.
- Liquid iron was considered to be iron without any impurities.

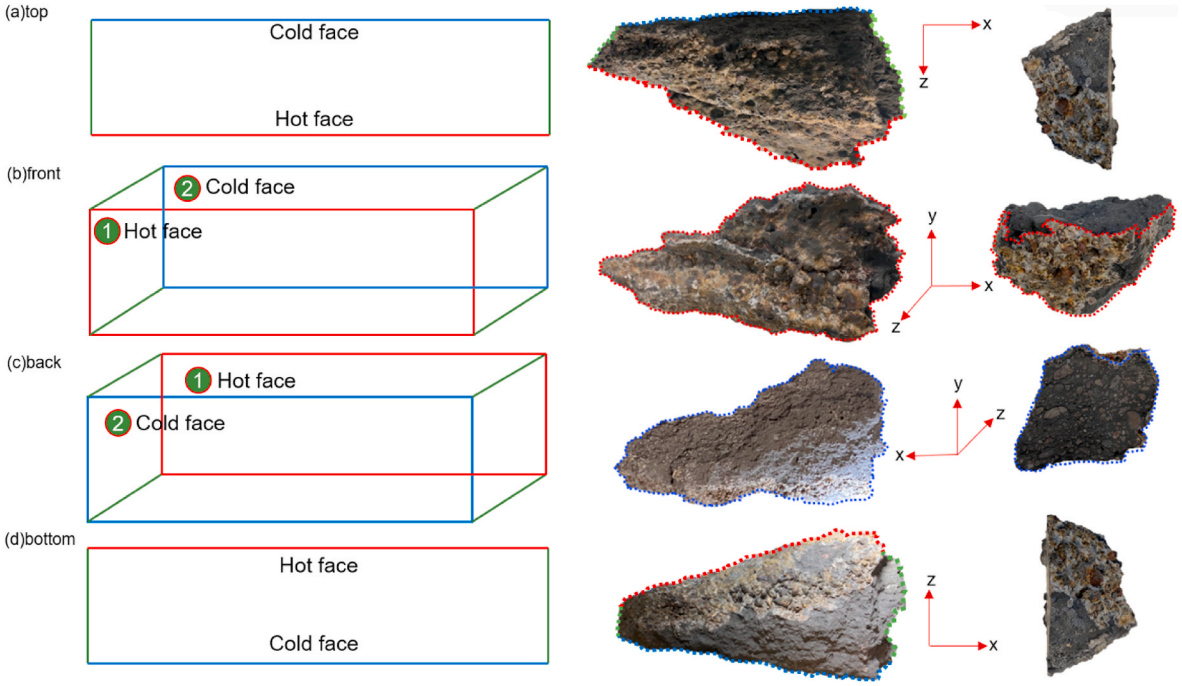

Fig. 9. Schema of post-mortem brick A-2.

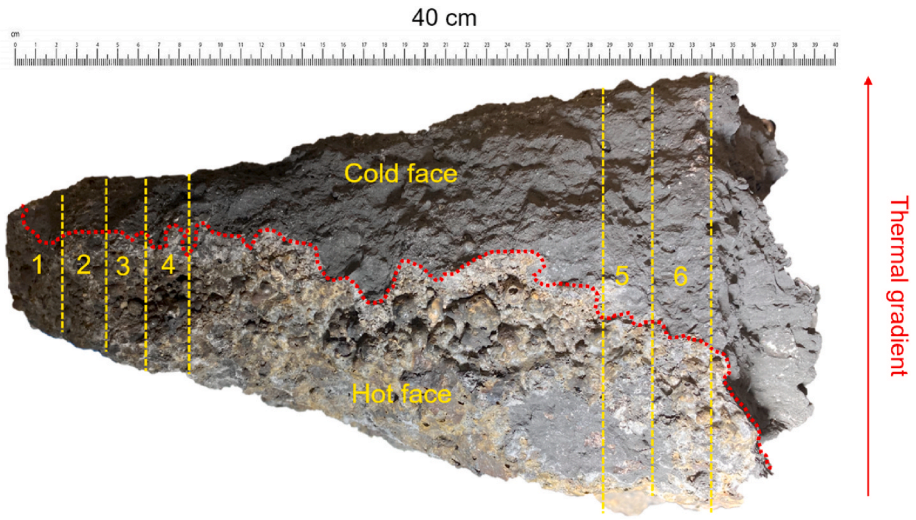

Fig. 10. Post-mortem sample A-2.

Fig. 11. Post-mortem castables delivered from locations in the middle of the runner, slag line B-1 (a); slag/iron line: B-2 (b), iron line: B-3 (c).

The databases implemented were "FactPS", "FToxid", and "FTmisc". Specifically, the liquid solution phases selected in the calculations were FToxid-SLAGA for liquid slag description and FT-misc-FeLQ for liquid metal iron. Calculations for solid phases included "FToxid-SPINC", "FToxid-MeO_A", "FToxid-Mel_A" and "FToxid-Mull" to represent the spinel, monoxide, melilite, and mullite solid solutions, respectively. All other solid phases were considered as stoichiometric compounds.

Two types of calculations were performed. The first type consisted of adding slag or iron stepwise into a system composed initially of pure ACS castable to calculate the nature and amount of the phases resulting from the equilibrium and thus simulate the corrosion reactions. The temperature was 1550 °C, and the pressure was 1 atm. This assumption is chosen first to simulate the higher temperature than the average temperature in the main runner's turbulence zone. Second, this assumption permits the system to reach closer to the equilibrium condition in the thermodynamic calculations. In these calculations, the amount of slag was increased from 0 g to 50 g by steps of 5 g. The proportion of iron in the castable was increased from 0 g to 10 g by steps of 1 g.

The second type of calculation consisted of cooling a mixture of 100 g of ACS castable and 5 g of slag from 1550 °C to 500 °C to simulate the solidification of the refractory impregnated by slag [21].

3. Results

3.1. Microstructural analysis of the turbulence zone of the runner

3.1.1. Slag transition area

Fig. 12(a) and (b) show the optical microscopic images of the hot face and cold face areas of sample A-1, which was located in zone A (turbulence) of the main runner, respectively. At first glance, the heterogeneous microstructure of ASC castables made of fine grains, called the matrix, and grains with different sizes, called aggregates, could be observed. Fig. 12 (a) shows the hot face on top of the infiltrated zone (white), highlighted with a yellow dashed line. The interface between the infiltrated and non-infiltrated zones (grey) is visible. The infiltration of slag seems to have stopped in the matrix. In Fig. 12 (b), the aggregates (large grains) and matrix (fine grains) are present, and there is no sign of infiltration of slag in this area. It can be seen that the depth of the slag varies from 0.5 mm to 0.2 mm in the infiltrated zone. This variation could be connected with the phase formed and the presence of carbon in the ASC castables matrix. The geometrical position of the post-mortem sample could be another important criterion to be considered. For instance, sample A-1 is located in the slag transition zone (slag line) of the main runner, where the atmosphere is always oxidizing since air is present in the slag line (Fig. 8).

Fig. 13 (a) and (b) show the SEM images (BSE mode) of the hot face and cold face of sample A-1, respectively. Fig. 13 (a) shows that the slag has partially infiltrated (orange dots) into the matrix where the SiC aggregates and carbon (C) are present. Nevertheless, as the distance from the hot face increases, the depth of the infiltration is reduced. Fig. 13 (b), indicates that ASC castables are made of alumina (Al_2O_3) and (SiC) aggregates together with fine alumina grains and carbon as the matrix. It has been suggested that some tin (Sn) and copper (Cu) impurities are present in the matrix. EDS chemical mapping was used in this study (Fig. 13) to understand the distribution of the main constitutive components of the ASC castables. The alumina aggregates are located on the upper and lower sides. In between, there are SiC aggregates with different grain sizes. The matrix comprises alumina and carbon, although fine carbon grains are accumulated and not well distributed in the matrix, as shown in the centre of Fig. 13(c).

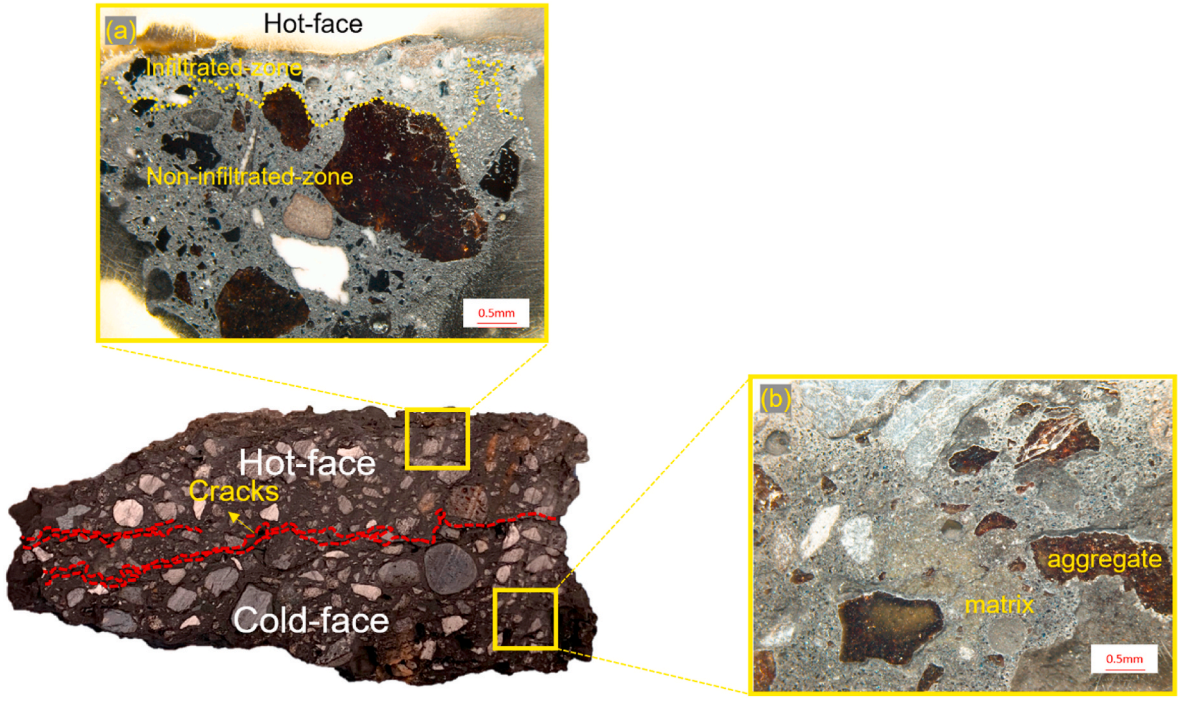

Fig. 12. Optical microscopy images of sample A-1 (a) hot face and (b) cold face.

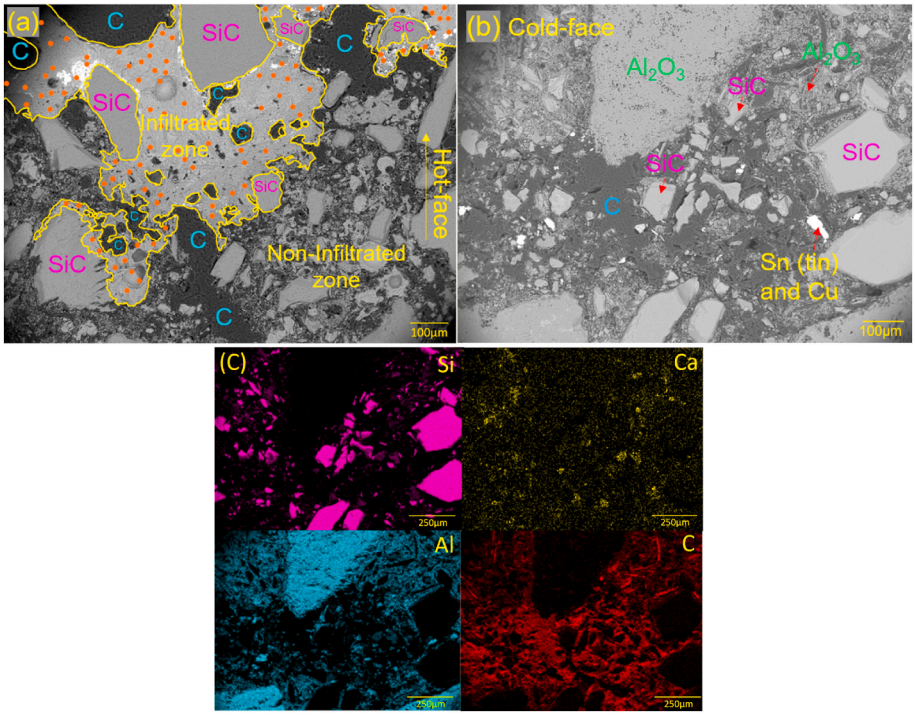

Fig. 13. BS images of the infiltrated zone: hot face (a), cold face (b), and mapping of cold face (c) of sample A-1.

Fig. 14 shows the images of EDS line mapping of different elements, such as Ca, Mg, Al, and C, from 0 μm (non-impregnated) to 600 μm (impregnated). According to Ref. [8], the profile of the Ca element could be used to characterize the level of slag penetration. Here, the high intensity of Ca and Mg starts from 600 μm to 300 μm, meaning that the depth of slag infiltration is about 300 μm. In contrast, in the non-impregnated area, the higher the intensity of Al is, the higher is the presence of alumina aggregates in the ASC castables.

3.1.2. Combined slag-metal transition area

Fig. 15 (a, b) shows the SEM images with lower and higher magnification, respectively, of the hot face of sample A-2. Sample A-2 was positioned in the slag/metal transition area during the lifetime of the main runner. Fig. 15 (a) shows that the crystallized slag is mainly gehlenite (Ca_2AlSiO_7). The in-situ spinel particles with rectangular shapes formed in the interaction within the infiltrated zone. The titanium particles have accumulated near the spinel ($MgAl_2O_4$) particles on the

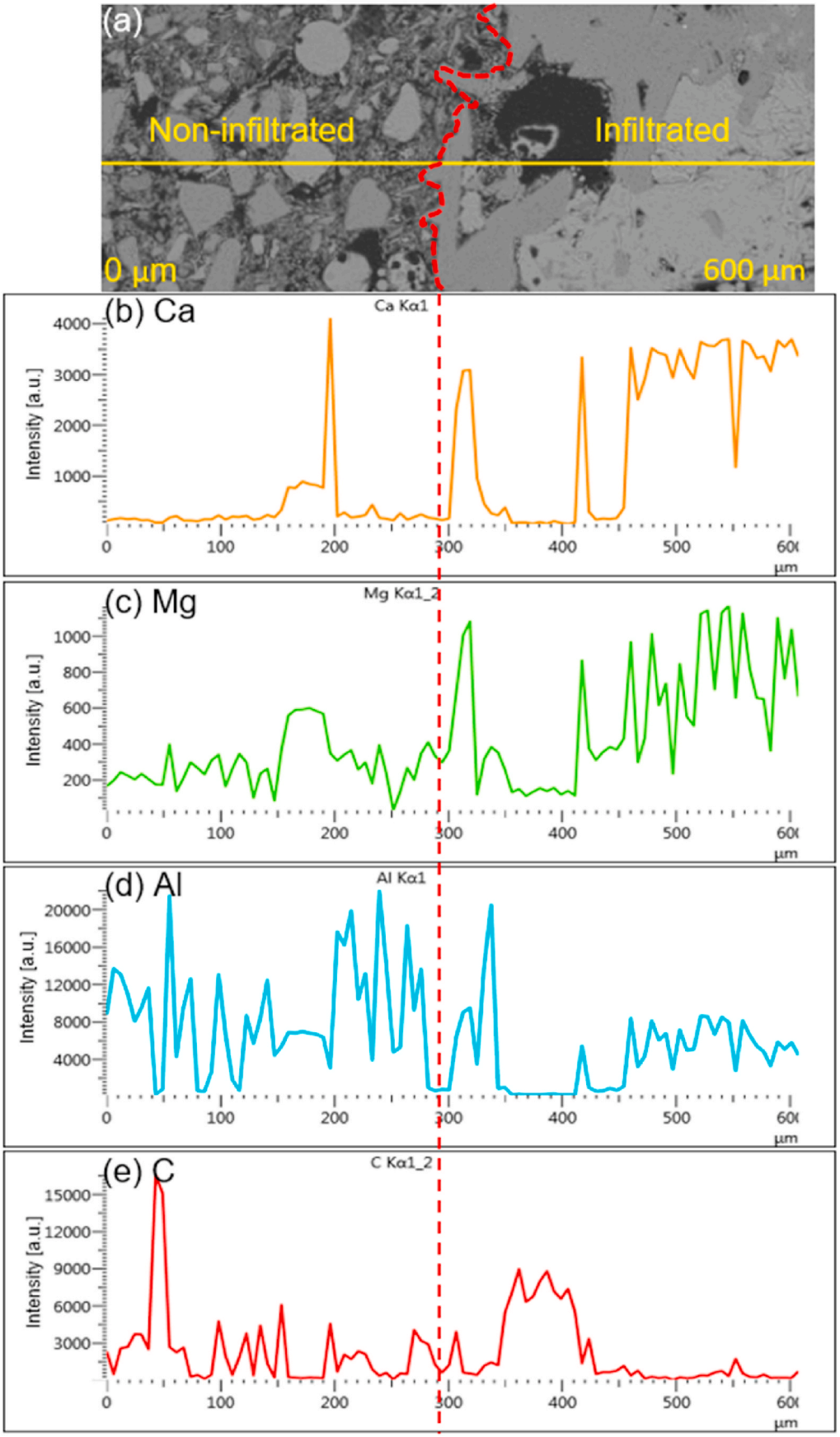

Fig. 14. Images of EDS line mapping of the hot face (a), elements Ca (b), Mg (c), Al (d), C (e).

upper right side. The thin interaction zone between slag and alumina aggregate is shown in Fig. 15(b). A calcium dialuminate (CA_2) layer has formed along the alumina aggregate. A limited amount of anorthite ($CaAl_2Si_2O_8$) has formed inside the infiltrated matrix made of gehlenite (C_2AS) near the calcium dialuminate (CA_2) layer.

3.2. Microstructural analysis of the middle zone of the runner

3.2.1. Slag transition area

Fig. 16 (a-d) shows the lower (a, b) and higher (c, d) magnifications of sample B-1 located in the slag line in the middle of a main runner. According to Fig. 16 (a, b), no slag has penetrated the matrix of the sample B-1. However, some iron inclusions have reacted with SiC grains and produced the Fe_3Si phase. The SEM images of sample B-1 in Fig. 16 are not similar to the microstructure observations of sample A-1 (Fig. 15). The mechanism of the oxidation of SiC and production of Fe_3Si will be explained in the discussion part. Fig. 16 (c,d) shows slag (around 50 μm) adhered on the hot face area, which is made of anorthite ($CaAl_2Si_2O_8$) and mullite ($Al_6Si_2O_{13}$). Moreover, fine grains of titanium (Ti) are distributed in the penetrated region. This suggests that Ti entered as impurities in the slag, depending on the kind of iron ore and the industrial process.

3.2.2. Combined slag-metal transition area

The SEM/EDS images of the hot face region of sample B-2 are shown in Fig. 17(a and b). Fine titanium (Ti) grains have accumulated near the alumina aggregate. Some anorthite phase is present in the matrix next to the hot face, showing the infiltration of slag into the matrix of sample B-2. Fig. 17(c) shows the alumina aggregate located in the hot face area. It seems that the vacancies of alumina aggregate are filled by secondary anorthite phases. It was possible to confirm this claim by checking the distribution of the Al, Si, Ca, and C elements shown in Fig. 17(d). The Si and Ca are distributed within the pores of alumina aggregate, and C is present in the black regions of the matrix. This suggests that slag infiltrated into sample B-2 in the middle of the runner, in the slag/metal zone, and created a phase with a low melting point, such as anorthite, within the porous alumina aggregates and in the matrix.

3.3. Microstructural analysis of the non-turbulence zone of the runner

For the sake of comparison between the different transition zones, Fig. 18 (a-d) shows the SEM/EDS images of the sample C-1 located in the non-turbulence zone (at the end) of the main runner. Fig. 18 (a) shows aggregates of silicon carbide (SiC) and alumina (Al_2O_3) distributed in the fine matrix. According to the EDS analysis and comparing the microstructure of sample C-1 to the original brick, it appears that slag penetration did not occur. However, iron (Fe) inclusions are present on the hot face of the sample C-1 ((Fig. 18 (b)). The iron inclusions are not only present in the matrix of the ASC castables, but are also located on the border of SiC grains (Fig. 18 (c)). The high magnifications of the border of SiC grains show that the Fe_3Si formed due to the reaction between the iron and the silicon carbide (Fig. 18 (d)).

3.4. Thermodynamic simulations

Fig. 19 shows the main stable phases during the addition of slag to 100 g of ASC castables at 1550 °C, where the amount of slag was increased from 0 g to 50 g by steps of 5 g (see section 2.5 for details of calculations). These calculations aim to represent the reaction of slag infiltrating into the refractory. It can be observed that, without slag in the system (i.e., for the x-axis value of 0 in Fig. 19), the calculation predicts the presence of two major phases, Al_2O_3 and SiC, and also small amounts (about 3 g) of anorthite ($CaAl_2Si_2O_8$) and mullite ($Al_6Si_2O_{13}$). The latter two phases probably do not represent the ASC castable's initial phase distribution, but we considered they could be disregarded due to their low concentration. Furthermore, these minor phases tend to disappear in contact with a small amount of slag.

Increasing the amount of slag causes the amount of alumina (Al_2O_3) to decrease from about 70 g to 30 g. This means that slag infiltration can induce the dissolution of large amounts of alumina aggregates. Conversely, silicon carbide (SiC) content is constant, which means that silicon carbide cannot dissolve into the slag. For large amounts of slag (above 30 g for 100 g of refractory), the formation of minor secondary phases (calcium hexaluminate ($CaAl_{12}O_{19}$) and spinel ($MgAl_2O_4$)) is predicted. Detecting such phases in corroded materials could then indicate a strongly corroded zone.

Fig. 20 shows the phases predicted to form during the cooling of the slag/refractory mixture (5 g of slag in 100 g of refractory) from 1550 °C to 500 °C. The phases formed are anorthite ($CaAl_2Si_2O_8$), hibonite ($CaAl_{12}O_{19}$), spinel ($MgAl_2O_4$), gehlenite ($Ca_2Al_2SiO_7$), grossular ($Ca_3Al_2Si_3O_{12}$), and sapphirine ($Mg_4Al_{10}Si_2O_{23}$). Specifically, freezing the liquid slag from 1550 °C predominantly forms the anorthite phase (reaching about 10 g at 1200 °C). The two other phases forming at high temperatures (around 1400 °C) are hibonite (~4 g) and spinel (~2 g). Then, the hibonite converts into gehlenite at around 1100 °C, while the spinel and the anorthite form 2 g of grossular and sapphirine below 700 °C. The grossular ($Ca_3Al_2Si_3O_{12}$) and sapphirine ($Mg_4Al_{10}Si_2O_{23}$) phases in the hot face region of post-mortem ASC samples were never evidenced in our characterizations, while our calculations showed that they should form a major phase after cooling below 700 °C. In contrast, the anorthite, spinel, and gehlenite phases were identified in our samples (Fig. 15 (a,b)). This suggests that the phase distribution in the samples was frozen at a temperature of about 1000 °C during cooling and that lower temperature solid-solid reactions did not occur because of kinetics restrictions.

Fig. 21 shows the effect of liquid metal iron on the ASC castables at 1550 °C. The proportion of iron in the castable was increased from 0 g to 10 g by steps of 1 g. Reaction between the alumina phase and liquid iron was absent (Fig. 21 (a)) but increasing the proportion of iron $Fe_{(l)}$ in equilibrium with the ASC castable decreased the SiC content proportionally, resulting in the formation of a liquid Fe-Si phase and solid carbon. The main reaction derived from this calculation is the direct

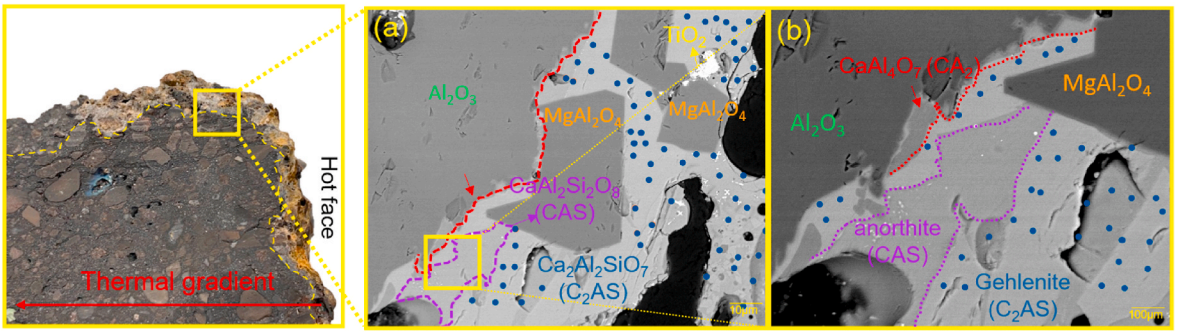

Fig. 15. SEM-BSE mode images of the hot face of sample A-2, low magnification (a) and high magnification (b).

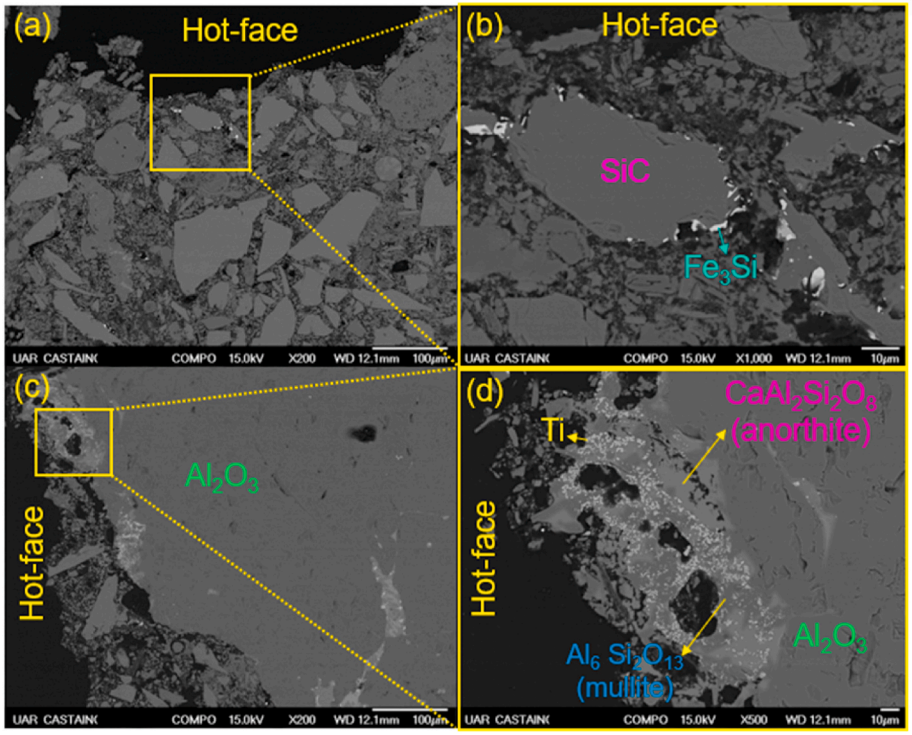

Fig. 16. BS images of sample B-1 from the middle of the runner slag line.

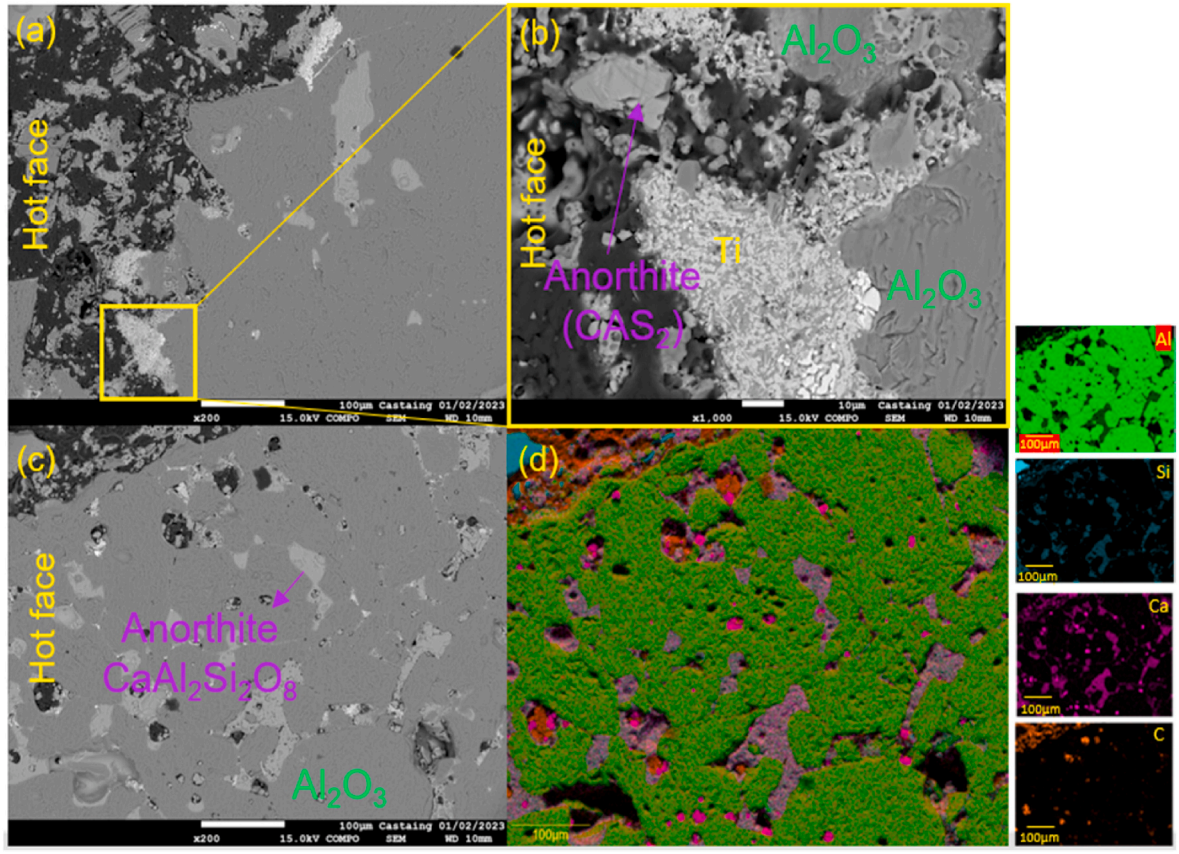

Fig. 17. BS SEM images (a–c) and elemental mapping (d) of sample B-2 located in the slag/metal line in the middle of the main runner.

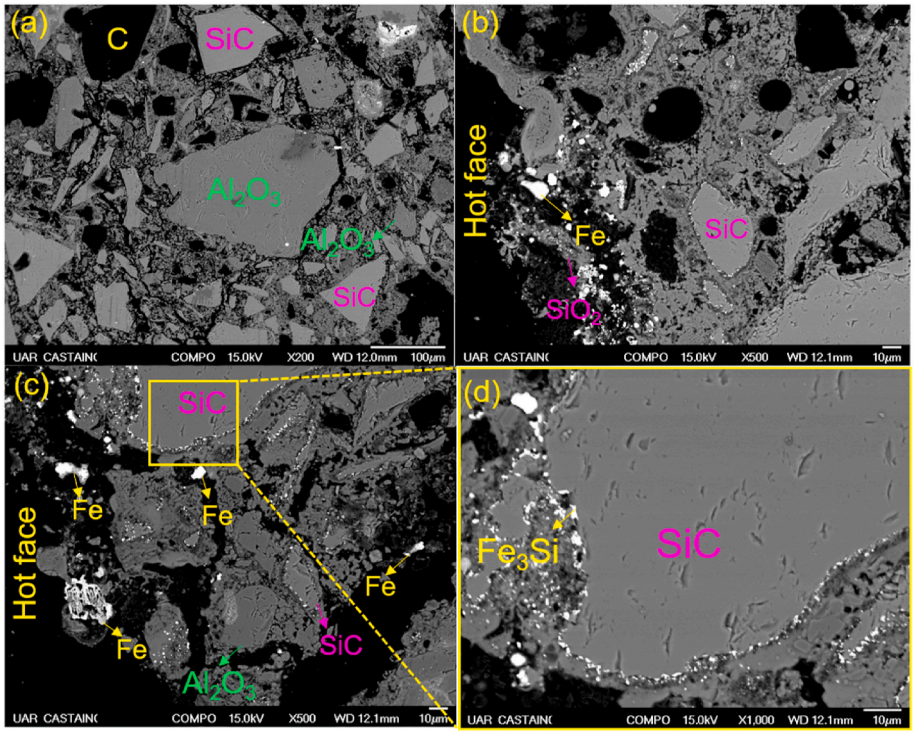

Fig. 18. BS SEM images of sample C-1 located in the non-turbulence zone of the main runner.

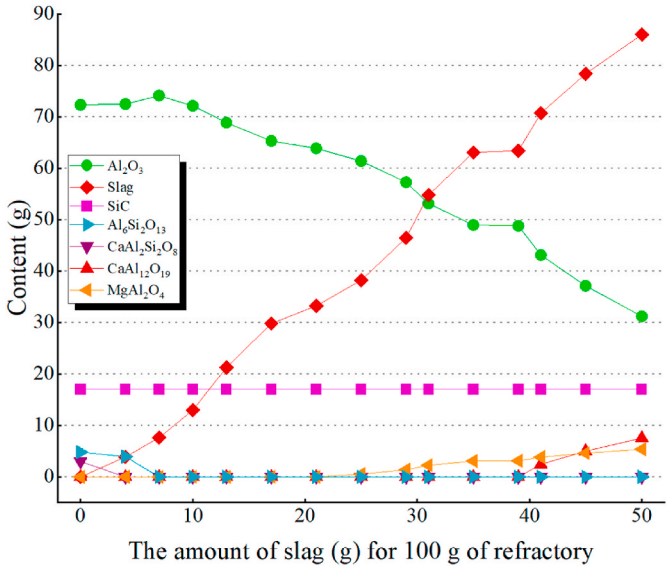

Fig. 19. Predicted stable phases in the refractory + slag system at 1550 °C.

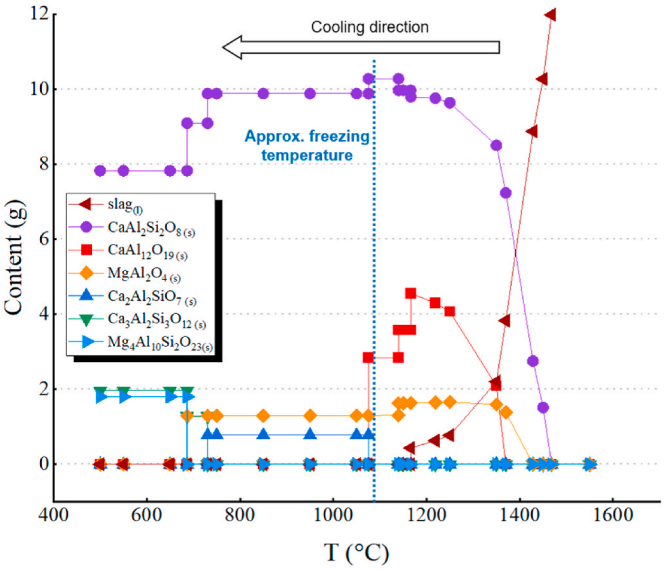

Fig. 20. Predicted formation of phases during slag/refractory system cooling.

decomposition of the SiC phase by liquid iron according to Eq. (1):

$$Fe_{(liq)} + SiC_{(s)} = Fe - Si_{(liq)} + C_{(s)} \quad \text{Eq. 1}$$

4. Discussion

4.1. Corrosion of the main runner by molten slag

Due to the extended penetration of slag within the matrix zone, it is suggested that the working atmosphere of sample A-2 is a weak reduced atmosphere (WRA) [3,5,23,24]. According to previous studies [3,25] in the WRA, slag penetrates the pores and reacts with the matrix to produce low melting point CAS phases such as anorthite ($CaAl_2Si_2O_8$) and gehlenite ($CaAlSi_2O_7$). According to Eq. (2) and Eq. (3), when the slag penetrates the matrix of ASC castables, CaO from the slag side reacts with Al_2O_3 and SiO_2 from the refractory side and forms aluminosilicate ternary phases such as anorthite ($CaAl_2Si_2O_8$) and gehlenite (Ca_2AlSiO_7) with low melting points of 1557 °C and 1527 °C, respectively.

$$CaO + Al_2O_3 + SiO_2 = CaO.Al_2O_3.2SiO_2 \quad \text{Anorthite} \quad (TM = 1557\ ^\circ C) \quad \text{Eq. 2}$$

$$2CaO + Al_2O_3 + SiO_2 = 2CaO.Al_2O_3.SiO_2 \quad \text{Gehlenite} \quad (TM = 1527\ ^\circ C) \quad \text{Eq. 3}$$

The other mechanism is the formation of calcium aluminates (CA_2

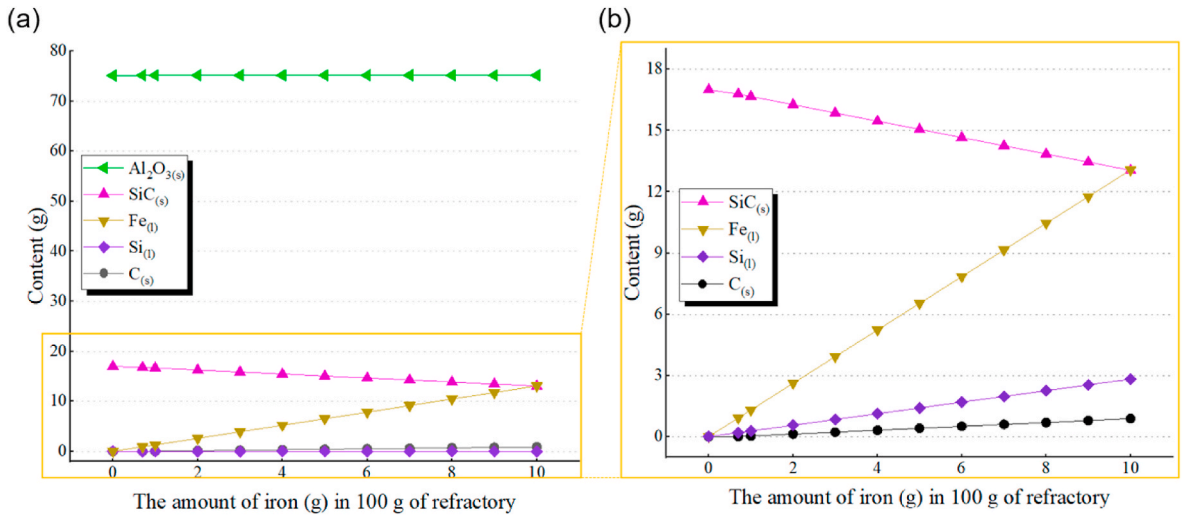

Fig. 21. (a) Predicted phase in the iron/refractory system at 1550 °C, and (b) magnification of the oxidation of SiC.

and CA_6) around the alumina aggregates (Fig. 13 (b)). Because of the reaction between the slag alumina aggregates, CaO (slag side) and Al_2O_3 (refractory side) react and form calcium aluminate layers around the alumina aggregates [26]. Depending on the time and temperature of corrosion, different calcium aluminate phases are generated, such as calcium mono-aluminate (CA), calcium dialuminate (CA_2), and calcium hexaluminate (CA_6), as shown in Eq. (4) and Eq. (6) [27].

$$CaO + Al_2O_3 = CaO.Al_2O_3 \quad \text{Calcium monoaluminate} \quad (\text{TM} = 1600\ ^\circ\text{C}) \qquad \text{Eq. 4}$$

$$CaO + 2Al_2O_3 = CaO.2Al_2O_3 \quad \text{Calcium dialuminate} \quad (\text{TM} = 1780\ ^\circ\text{C}) \qquad \text{Eq. 5}$$

$$CaO + 6Al_2O_3 = CaO.6Al_2O_3 \quad \text{Calcium hexaluminate} \quad (\text{TM} = 1830\ ^\circ\text{C}) \qquad \text{Eq. 6}$$

As shown in Fig. 15 (b), a thin layer of calcium dialuminate (CA_2) was formed around the alumina grain in the infiltrated zone of the matrix of sample A-2. According to Refs. [1,28–30], formation of calcium aluminate layers around alumina grains could be advantageous for the corrosion resistance of ASC castable. According to Refs. [11,13,25, 29–31], the CA_2 acts as a protective layer and prevents further reaction between CaO and Al_2O_3. As a result, the corrosion rate of WFA aggregate by slag decreases. Nevertheless, it should be mentioned that alumina and calcium dialuminate are incompatible thermodynamically and, when the temperature is increased or the corrosion time extended, they react with each other and form calcium hexaluminate (CA_6). This is why the thermodynamic calculations shown in Fig. 19 predicted calcium hexaluminate as a stable phase instead of calcium dialuminate.

The formation of a spinel layer around the alumina aggregates eliminates the further corrosion of alumina aggregates and decreases the erosion of castables [32]. The MgO from the slag side reacts with fine alumina present in the matrix of the ASC castables and, based on Eq. (7), magnesium aluminate ($MgAl_2O_4$) forms within the penetrated zones of the matrix (Fig. 13 (a,b)). Since spinel is extremely resistant to corrosion, the formation of fine in-situ spinel grains is desirable for the corrosion resistance of ASC castables. However, it should be noted that excessive spinel formation could be disadvantageous since it is associated with volume expansion [25].

$$MgO + Al_2O_3 = MgO.Al_2O_3 \quad \text{Spinel} \quad (\text{TM} = 2135\ ^\circ\text{C}) \qquad \text{Eq. 7}$$

Here, the microstructural analysis of the hot face region (Figs. 15–17) and the thermodynamic results of the slag/refractory system (Figs. 19 and 20) are in line with each other. Regarding samples A-1 and A-2, the thermodynamic results are in accordance with experimental SEM/EDS results.

The SEM images show that the calcium dialuminate (CA_2) and spinel grains are present in the hot face. Based on the FactSage results, calcium hexaluminate and spinel were formed at 1550 °C in the final steps by increasing the slag in the ASC castables. Also, they were formed during the cooling procedure of slag-ASC castable. The formation mechanism of calcium aluminates, e.g., CA, CA_2, CA_6, is extensively explained in Refs. [27,28] and does not fall within the domain of interest of this study.

According to the thermodynamic results, calcium hexaluminate should form at 1550 °C when a large amount of slag reacts with alumina. Furthermore, it is also a stable phase during the cooling steps, due to the infiltration of Ca^{+2} ions from the slag side into the calcium dialuminate layers [27,28]. According to the SEM images shown in Fig. 15, the calcium dialuminate layer was formed around the alumina aggregates of sample A-2 rather than the calcium hexaluminate. It can be concluded that the system did not reach equilibrium conditions to form calcium hexaluminate (CA_6) but achieved the formation of calcium dialuminate (CA_2).

The SEM image in Fig. 15 (b) shows that the anorthite and gehlenite were formed in the infiltrated matrix of sample A-2, which is in accordance with the thermodynamic simulations shown in Fig. 20. According to the thermodynamic results, during the cooling of slag, first the anorthite started to form at 1500 °C, and the gehlenite appeared at 1100 °C. Hence, it is concluded that the formation of ternary phases such as gehlenite and anorthite in the infiltrated matrix progresses during the slag's cooling and not at the working temperature.

According to Figs. 16 and 17, slag reacted partially with the matrix of ASC castables without measurable infiltration. Anorthite and mullite were formed in the hot face regions of samples B-1 and B-2 located in the slag and slag-metal lines of the runner, respectively. This is consistent with thermodynamic simulations predicting that anorthite and mullite could be formed in the first reaction steps between the slag and ASC castables. Moreover, the presence of calcium hexaluminate or spinel was not confirmed by SEM/EDS analysis. This point revealed that, unlike samples A-1 and A-2, samples B-1 and B-2 have a corrosion process that is not very advanced.

4.2. Corrosion of the main runner by molten iron

According to Eq. (1) derived from our thermodynamic calculations, the SiC phase can be decomposed by liquid iron, with the dissolution of Si in a molten Fe- Si phase and the formation of solid carbon (Fig. 21). This mechanism is consistent with the SEM images in Figs. 16 (b) and

Fig. 17(b-d), which show that iron inclusions are present in the matrix of samples B-1 and C-1 and Fe_3Si nodules are present around the SiC aggregates. Fan et al. [8] Also reported was the formation of Fe_3Si thin layers in Al_2O_3-SiC-C samples exposed to 10 h of heat treatment under a reduced atmosphere at 700 °C. The formation of Fe_3Si is likely to have been caused by the solidification of the Fe-Si liquid phase during the cooling of the refractory. Therefore, it can be concluded that the oxides present in the ASC castables are likely to react with oxides of slag, while silicon carbide and carbon could be dissolved by molten iron during the corrosion process of ASC castables.

4.3. Corrosion of turbulence zone by the mixture of molten slag/iron

Fig. 22 shows the schema of the corrosion/erosion mechanism of ASC castables by slag/iron in the turbulence zone of the main runner. The slag-iron transition area is the critical area in the whole runner since it determines the lifetime of the main runner.

In the slag corrosion zone, the oxides of the ASC castables gradually dissolve into the slag, and a new phase, such as spinel ($MgAl_2O_4$), akermanite ($CaMgSi_2O_7$), gehlenite ($CaAl_2SiO_7$) or anorthite ($CaAl_2Si_2O_8$) appears on the slag-sample interface and calcium hexaluminate (CA_6) layers form around alumina aggregates. Generally, spinel and CA_6 layers inhibit slag corrosion unless slag flow washes them away. It must be mentioned that the formation of spinel and CA_6 is coupled with volumetric expansion and, in case of excessive formation, affords a channel for further slag erosion [28,33]. Since iron has higher liquidity than slag, only a little iron remains on the carbon located on the interface. This carbon conserved on the interface could efficiently deter further slag corrosion because of its poor wettability with the molten slag [6].

Afterwards, the freshly produced phase and other oxides, such as SiO_2, enter the slag-iron interface. The SiO_2 reacts with carbon, which is already present in molten iron, to form CO bubbles, and the CO bubbles produced raise the reaction-specific surface area. As a result, the speed of reduction of SiO_2 in the interaction area increases, providing further channels for iron erosion and producing [Si]. Conversely, in the iron erosion zone, the carbon of ASC castable dissolves into molten iron. Also, SiO_2 from the slag side reacts with carbon in the molten iron and generates [Si]. The consumption of carbon from molten iron could accelerate the dissolution of carbon from the refractory sample into iron and increase the erosion of alumina-carbon refractory brick.

As in Fig. 7, the CFD results showed that, when the melted slag and iron drain from the taphole into the runner, there is a “back-flow” incident in the turbulence zone of the main runner. In other words, in the main runner’s turbulence zone, the mixture of slag and iron is refreshed rapidly due to the dynamic flow and participates in the wear of the walls of the main runner. Based on the explanation above, the backflow intensifies the erosion of the ASC castables and results in higher wear in the turbulence zone of the main runner.

The ASC castables in the working lining of the turbulence zone are constantly exposed to the floating slag-iron mixture (S-I). In the S-I interface, a slag film is formed when the S-I mixture passes between the ASC castables and the molten iron. The oxide of the ASC castables dissolves into slag film and exposes carbon with poor wettability to the slag on the S-I interface. The carbon immediately comes into contact with the iron and dissolves or oxidizes quickly. Consequently, the proportion of oxides with poor wettability to iron increases at the S-I interface and the dissolve into the slag film. This procedure repeats rapidly in the turbulence zone. Therefore, the dynamic rotating of slag-metal liquid results in intensive erosion in the turbulence zone of the main runner.

5. Conclusion

Based on the CFD simulations, the main runner of the blast furnaces was divided into different zones concerning the movement of molten media (slag and iron), namely: the turbulence zone (A), the middle zone (B), and the non-turbulence zone (C). The “flow-back” co-circulations of the stream of the slag-iron mixture in the turbulence zone (A) exposed the walls of the main runner to the refreshed corrosion medium. The microstructural investigations of the post-mortem Al_2O_3-SiC-C (ASC) samples from different zones of the runner were carried out by SEM/EDS techniques. Next, the experimental results were compared with those simulated by the thermodynamic software of FactSage. It was found that the simulated results correlated with the results obtained from the microstructural characterizations of the post-mortem samples of ASC castables.

The microstructural investigations showed that the depth of infiltration of slag in sample A-2 (from the turbulence zone) was about 300 μm whereas no infiltrated area was observed in the matrix of sample C-1 (from the non-turbulence zone). However, some iron inclusions were found in its hot-face regions. The presence of gehlenite, anorthite, and solid solutions of spinel was confirmed in the infiltrated regions of samples A-1 and A-2 matrix. Moreover, it was found that the mullite and anorthite were present in the infiltrated regions of samples B-1 and B-2.

According to the thermodynamic results, the slag mainly reacted with alumina from the refractory side, not with silicon carbide or carbon. The dissolution of silicon carbide was attributed to the presence of iron. The simulation of the cooling steps of the slag-refractory system showed that the aluminosilicate ternary phases with low melting points, such as gehlenite ($CaAlSi_2O_7$) and anorthite ($CaAl_2Si_2O_8$), as well as calcium hexaluminate ($CaO.6Al_2O_3$) and solid solutions of spinel ($MgAl_2O_4$) were formed during the cooling steps of the slag/refractory. These phases confirmed the slag penetration within the matrix of samples A-1 and A-2 from the main runner’s slag line and slag-metal line. However, mullite formation in the matrix of samples B-1 and B-2 located in the middle zone showed that the corrosion was not as advanced as in the turbulence zone of the runner. The iron inclusions were present in the matrix of sample C-1, although they formed a thin layer of Fe_3Si on the border of SiC during the cooling procedure.

The formation of gehlenite and anorthite with low melting

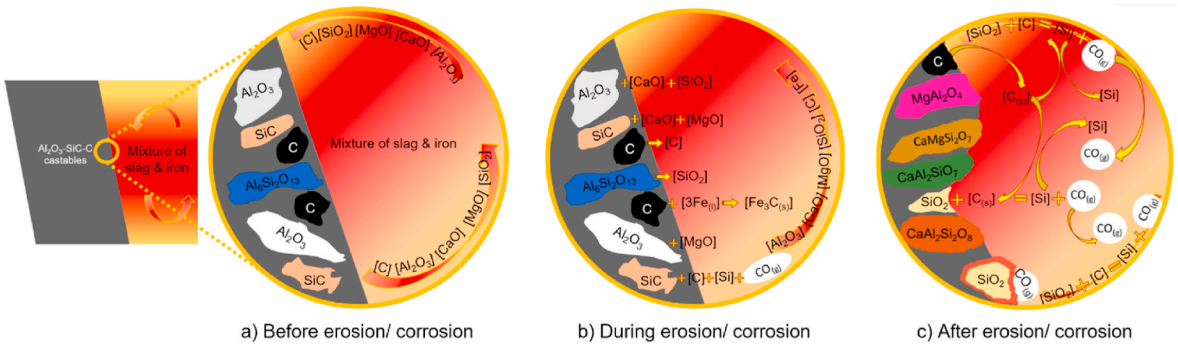

Fig. 22. Schematic view of corrosion mechanism in the turbulence zone of the main runner of a blast furnace.

temperatures in the infiltrated regions of the matrix could extend the penetration of slag at high temperatures (1550-1600 °C). At the same time, forming a layer of calcium hexaluminate around the alumina aggregate could minimize the dissolution of the alumina in the slag. Moreover, the in-situ formation in the matrix of solid solutions of spinel with high corrosion resistance could eliminate further corrosion of ASC castables. The silicon carbide in the B-1 and C-1 samples from the middle and non-turbulence zones of the runner could dissolve into the molten iron. Therefore, it can be concluded that slag and iron play complementary roles in the corrosion mechanisms of ASC castables. While the slag penetrates and reacts with the alumina aggregates, iron dissolves the silicon carbide and facilitates further slag penetration within the matrix of ASC castables.

References

[1] Chien Nan Pan, Corrosion mechanism analysis of Al2O3-SiC-C castable, Adv. Sci. Technol. 92 (2014) 258–263.

[2] Pingyi Zhou, Xin Qiu, Zhongtao Luo, Xinhong Liu, Shaowei Zhang, Quanli Jia, Effect of firing atmosphere on the microstructure and properties of Al2O3–SiC–C castables, Ceram. Int. 47 (10) (2021) 14280–14289.

[3] Muhan Wu, Ao Huang, Ding Chen, Lvping Fu, Huazhi Gu, Effect of carbon black on corrosion resistance of Al2O3–SiC–C castables to SiO2–MgO slag, Ceram. Int. 48 (10) (2022) 13659–13664.

[4] A. Gallet-Doncieux, Ouziyine Bahloul, Christian Gault, Marc Huger, Thierry Chotard, Investigations of SiC aggregates oxidation: influence on SiC castables refractories life time at high temperature, J. Eur. Ceram. Soc. 32 (4) (2012) 737–743.

[5] Muhan Wu, Ao Huang, Shuang Yang, Huazhi Gu, Lvping Fu, Guangqiang Li, Hongyuan Dong, Corrosion mechanism of Al2O3–SiC–C refractory by SiO2–MgO-based slag, Ceram. Int. 46 (18) (2020) 28262–28267.

[6] Shijie Wang, Pingyi Zhou, Xin Liu, Junyan Cui, Xinhong Liu, Shaowei Zhang, Quanli Jia, Effect of modified coal tar pitch addition on the microstructure and properties of Al2O3–SiC–C castables for solid waste incinerators, Ceram. Int. 48 (14) (2022) 20778–20790.

[7] Haibin Zuo, Cong Wang, Yingli Liu, Dissolution behavior of a novel Al2O3-SiC-SiO2-C composite refractory in blast furnace slag, Ceram. Int. 43 (9) (2017) 7080–7087.

[8] Xiaoyue Fan, Kexin Jiao, Jianliang Zhang, Ruiqi Cao, Rusheng He, Kaidi Wang, Study on physicochemical properties of Al2O3SiCC castable for blast furnace, Ceram. Int. 45 (11) (2019) 13903–13911.

[9] G.L. Xuekun Tian, et al., Replacement of different sizes of corundum with andalusite in iron runner castables, 61st International Colloquium on Refracractories (2018) 219–221, 2018.

[10] Venkatesh Pilli, Ritwik Sarkar, Nanocarbon containing Al2O3–C continuous casting refractories: effect of graphite content, J. Alloys Compd. 735 (2018) 1730–1736.

[11] V.G. Domiciano, A.R. Ollmann, E.I. Clemente, A.K. Duarte, M.A.M. Brito, Challenges of blast furnace casthouse: failure analysis of main runner refractory castable, in: Proceedings of the Unified International Technical Conference on Refractories (UNITECR 2013), John Wiley & Sons, Inc, Hoboken, NJ, USA, 2014, pp. 553–558.

[12] Yichong Li, Huizhong Zhao, Han Zhang, Dunxiang Pan, Yunkang Feng, Yuangao Li, Xinquan Wang, Yindong Guo, Enhancement and explosion-proof mechanism of aluminum fiber addition in Al2O3–SiC–C castables for iron runner, Ceram. Int. 45 (17) (2019) 22723–22730.

[13] A.P. Luz, J.H. Gagliarde, C.G. Aneziris, V.C. Pandolfelli, B4C mineralizing role for mullite generation in Al2O3-SiO2 refractory castables, Ceram. Int. 43 (15) (2017) 12167–12178.

[14] Hossain Sarpoolaky, Shaowei Zhang, Bernard Barry Argent, William Edward Lee, Influence of grain phase on slag corrosion of low-cement castable refractories, J. Am. Ceram. Soc. 84 (2) (2001) 426–434.

[15] Haibing Fan, Yawei Li, Shaobai Sang, Microstructures and mechanical properties of Al2O3–C refractories with silicon additive using different carbon sources, Mater. Sci. Eng., A 528 (7–8) (2011) 3177–3185.

[16] Zhe Chen, Yan Wen, Stefan Schafföner, Yawei Li, Nan Li, Microstructure and mechanical properties of lightweight Al2O3-C refractories using different carbon sources, J. Alloys Compd. 862 (2021), 158036.

[17] Using the CaO-Al2O3-SiO2 ternary phase diagram | Chegg.com. https://www.chegg.com/homework-help/questions-and-answers/using-cao-al2o3-sio2-ternary-phase-diagram-complete-following-table-compounds-75-points-st-q62983645. (Accessed 8 July 2023).

[18] Jacques Poirier, Jeffrey D. Smith, In-Ho Jung, Youn-Bae Kang, Nicolas Eustathopoulos, Éric Blond, Michel Rigaud, Corrosion Of Refractories: the Fundamentals, Göller Verlag, Baden-Baden, Germany, 2017.

[19] Francis Lacombe, Vérification et validation d'une loi de paroi consistante du modèle de turbulence k-ω SST, Ecole Polytechnique, Montreal (Canada), 2017.

[20] C.W. Bale, E. Bélisle, P. Chartrand, S.A. Decterov, G. Eriksson, A.E. Gheribi, K. Hack, I.H. Jung, Y.B. Kang, J. Melançon, A.D. Pelton, Reprint of: FactSage thermochemical software and databases, 2010–2016, Calphad 55 (2016) 1–19.

[21] A.P. Luz, V.C. Pandolfelli, Thermodynamic evaluation of SiC oxidation in Al2O3–MgAl2O4–SiC–C refractory castables, Ceram. Int. 36 (6) (2010) 1863–1869.

[22] Ansys fluent | fluid simulation software. https://www.ansys.com/products/fluids/ansys-fluent. (Accessed 21 June 2023).

[23] Shoulei Yang, Guoqing Xiao, Donghai Ding, Jianying Gao, Effect of in-situ carbon containing calcium aluminate cement on properties of Al2O3-SiC-C based trough castables, Journal of Asian Ceramic Societies 8 (1) (2020) 162–169.

[24] Jiuhong Ma, Huizhong Zhao, Jun Yu, Han Zhang, Yichong Li, Lida Shi, Yi Zhao, Jian He, The critical role of aggregate microstructure in thermal shock resistance and slag resistance of Al2O3–SiC–C castable, Ceram. Int. 48 (8) (2022) 11644–11653.

[25] Luz, A. P., AG Tomba Martinez, M. A. L. Braulio, and V. C. Pandolfelli. "Thermodynamic evaluation of spinel containing refractory castables corrosion by secondary metallurgy slag." Ceram. Int. 37, no. 4 (2011): 1191-1201..

[26] Shoulei Yang, Guoqing Xiao, Donghai Ding, Xinmin Yu, Li Guan, Jianying Gao, Improved corrosion resistance of Al2O3-SiC-C castables through in situ carbon containing aluminate cement as binder, Int. J. Appl. Ceram. Technol. 17 (3) (2020) 1044–1051.

[27] de Bilbao, Emmanuel, Mathieu Dombrowski, Pilliere Henry, Jacques Poirier, Time-resolved high-temperature X-ray diffraction for studying the kinetics of corrosion of high-alumina refractory by molten oxides, Corrosion Sci. 139 (2018) 346–354.

[28] Sina Darban, Camille Reynaert, Maciej Ludwig, Ryszard Prorok, Ilona Jastrzębska, Jacek Szczerba, Corrosion of alumina-spinel refractory by secondary metallurgical slag using coating corrosion test, Materials 15 (10) (2022) 3425.

[29] M.A.L. Braulio, AG Tomba Martinez, A.P. Luz, C. Liebske, V.C. Pandolfelli, Basic slag attack of spinel-containing refractory castables, Ceram. Int. 37 (6) (2011) 1935–1945.

[30] M.A.L. Braulio, AG Tomba Martinez, A.P. Luz, C. Liebske, V.C. Pandolfelli, Basic slag attack of spinel-containing refractory castables, Ceram. Int. 37 (6) (2011) 1935–1945.

[31] AG Tomba Martinez, A.P. Luz, M.A.L. Braulio, V.C. Pandolfelli, CA6 impact on the corrosion behavior of cement-bonded spinel-containing refractory castables: an analysis based on thermodynamic simulations, Ceram. Int. 41 (3) (2015) 4714–4725.

[32] M.A.L. Braulio, M. Rigaud, A. Buhr, C. Parr, V.C. Pandolfelli, Spinel-containing alumina-based refractory castables, Ceram. Int. 37 (6) (2011) 1705–1724.

[33] Kexin Jiao, Xiaoyue Fan, Jianliang Zhang, Kaidi Wang, Yongan Zhao, Corrosion behavior of alumina-carbon composite brick in typical blast furnace slag and iron, Ceram. Int. 44 (16) (2018) 19981–19988.